

Imaging individual barium atoms in solid xenon for barium tagging in nEXO

nEXO Collaboration*

Double- β -decay involves the simultaneous conversion of two neutrons into two protons, and the emission of two electrons and two neutrinos; the neutrinoless process, although not yet observed, is thought to involve the emission of the two electrons but no neutrinos. The search for neutrinoless-double- β -decay probes fundamental properties of neutrinos, including whether or not the neutrino and antineutrino are distinct particles. Double- β -decay detectors are large and expensive, so it is essential to achieve the highest possible sensitivity with each study, and removing spurious contributions ('background') from detected signals is crucial. In the nEXO neutrinoless-double- β -decay experiment, the identification, or 'tagging', of the ¹³⁶Ba daughter atom resulting from the double- β decay of ¹³⁶Xe provides a technique for discriminating background. The tagging scheme studied here uses a cryogenic probe to trap the barium atom in a solid xenon matrix, where the barium atom is tagged through fluorescence imaging. Here we demonstrate the imaging and counting of individual barium atoms in solid xenon by scanning a focused laser across a solid xenon matrix deposited on a sapphire window. When the laser irradiates an individual atom, the fluorescence persists for about 30 seconds before dropping abruptly to the background level—a clear confirmation of one-atom imaging. Following evaporation of a barium deposit, the residual barium fluorescence is 0.16 per cent or less. Our technique achieves the imaging of single atoms in a solid noble element, establishing the basic principle of barium tagging for nEXO.

The search for neutrinoless-double- β -decay $(0\nu\beta\beta)$ offers a window into the nature of neutrinos. Observation of such decay would suggest that neutrinos are Majorana particles (meaning that the neutrino and antineutrino are the same particle); it would also demonstrate violation of lepton number conservation, and help to determine the absolute neutrino mass ¹. The EXO-200 experiment is searching for $0\nu\beta\beta$ in 136 Xe, using 110 kg of active liquid xenon (LXe) enriched to 80.6% 136 Xe in a time-projection chamber (TPC). Two-neutrino double- β decay $(2\nu\beta\beta)$ of 136 Xe has been observed in EXO-200, and its half-life is measured 2 to be $T_{1/2}^{2\nu\beta\beta}=2.165\pm0.016(\text{stat})\pm0.059(\text{sys})\times10^{21}$ yr (where stat and sys refer to the statistical and systematic errors). The most recent EXO-200 $0\nu\beta\beta$ search sets a limit on the half-life ($T_{1/2}^{0\nu\beta\beta}$) of more than 1.8×10^{25} yr (90% confidence limit), which corresponds to an effective Majorana neutrino mass $\langle m_{\nu_e} \rangle$ of less than 147–398 meV, depending on nuclear matrix element calculations ³.

A 136 Xe TPC provides a unique opportunity to tag the daughter 136 Ba at the site of a double- β -decay event. Implementing this barium tagging would improve $0\nu\beta\beta$ sensitivity by effectively eliminating all backgrounds except $2\nu\beta\beta$ (ref. 4). Barium tagging is being investigated for a future upgrade of the next-generation LXe experiment, nEXO, based on five tonnes of enriched xenon 5,6 . Initial results have been reported regarding methods of barium tagging in LXe 7,8 and in a xenon-gas TPC 9 . The NEXT collaboration has also reported images of single Ba $^{2+}$ ions in fluorescent dye molecules from a dilute deposit of barium perchlorate salt solution 10 .

In this study, we present a major step towards the realization of barium tagging in solid xenon (SXe) for nEXO⁷. In this method, a cryogenic probe would be moved to the position of the $0\nu\beta\beta$ candidate event in LXe, and the daughter atom or ion would be captured in a small amount of SXe on a sapphire window at the end of the probe^{11,12}. It would then be detected by its laser-induced fluorescence in the SXe. It is expected that a Ba²⁺ ion will convert to Ba⁺ in LXe, as the LXe

conduction band gap is less than the ionization potential for Ba $^+$ (ref. 4). Neutralization to barium may also occur in the charge cloud following a $\beta\beta$ event. A study of ^{214}Bi daughters of ^{214}Pb β -decay in EXO-200 reported that $76\pm6\%$ of these daughters are ionized, with negligible subsequent neutralization after many minutes 13 . Thus, a large fraction of ^{136}Ba 0 $\nu\beta\beta$ daughters is expected to be in the singly ionized state in LXe. Whether or not the ^{136}Ba will remain ionized in SXe on a cold probe is not yet known.

There has been substantial progress in understanding the spectroscopy of barium in SXe^{7,14,15}. Through theoretical modelling, the strongest fluorescence peaks at 577 nm and 591 nm have been identified as barium atoms in five-atom and four-atom vacancy sites in the SXe matrix¹⁵. These two fluorescence peaks bleach fairly rapidly at high laser intensity—for example, when using a focused laser beam⁷. Obtaining large numbers of photons from single barium atoms in these matrix sites would benefit from a method to overcome bleaching, for example, with repumping lasers. The barium emission peak at 619 nm, although not reported for some deposits made at 10 K (refs 14,15), is more prominent in annealed deposits or deposits that were made at higher temperature and observed at 10 K (ref. ⁷ and J. G. McCaffrey, personal communication). The excitation spectrum for this peak is shown in Extended Data Fig. 1, along with that of a possible companion emission line at 670 nm. It does not exhibit the resolved Jahn-Teller triplet structure of the excitation spectra of the peaks at 577 nm and 591 nm. The peak at 619 nm is attributed in our work to barium atoms in a single-vacancy site. This peak exhibits less bleaching than do the emission peaks at 577 nm and 591 nm, and is thus more amenable to the imaging of single barium atoms. The apparatus for depositing and observing Ba/Ba⁺ deposits in SXe is described in ref. ⁷, and important components are shown in Fig. 1.

Here we report the imaging of single barium atoms in SXe via the fluorescence peak at 619 nm. This is, to our knowledge, the first time that single atoms have been imaged in a solid noble-element matrix. Images

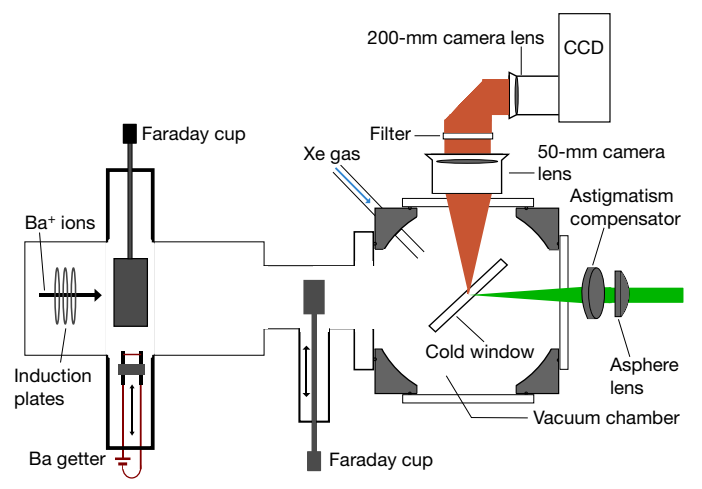


Fig. 1 | Experimental setup for Ba/Ba⁺ imaging in solid xenon. The two sources of barium are shown on the left: a BaAl4 getter and a pulsed beam of Ba⁺ ions. The ion pulses are measured with a set of induction plates and two Faraday cups, which ensure the alignment of the ion beam. Xenon gas is condensed on a 0.5-mm-thick cold sapphire window tilted at 45°, mounted to a cryostat cold finger. The xenon gas enters the cryostat via a tube pointed at the upper window surface. Pulses of Ba⁺ ions are incident during the xenon deposit. The neutralized barium atoms are excited by a dye laser focused by an asphere lens with a focal length of 7.9 cm. An optical flat is used to compensate for the astigmatism introduced by the tilt of the sapphire window. The asphere lens is mounted on piezoelectric translation stages, allowing the laser to be precisely moved across the sample. The fluorescence is observed from above, collimated by a 50-mm camera lens and focused onto a liquid-nitrogen-cooled CCD camera by a 200-mm camera lens. The fluorescence is filtered to pick out the emission range of interest.

of single molecules of DBATT dye in solid krypton and xenon¹⁶, as well as Mg-TAP molecules in solid xenon¹⁷, have been obtained previously.

Fixed laser images

The barium fluorescence in a given deposit is determined by summing the counts in a 4×4 pixel area that encloses the laser spot, and subtracting the SXe-only background. The background is measured by averaging the summed charge-coupled-device (CCD) counts in the focused laser region from the prior SXe-only deposit, and following SXe-only deposit for each Ba⁺ deposit. A typical background level is about 1,000 counts per milliwatt-second. The observed barium counts per milliwatt-second of laser exposure are plotted against the number of Ba⁺ ions deposited in the laser region in Fig. 2a. Given that the neutralization fraction is not known, the number of barium atoms in the laser beam is less than or equal to the number of ions deposited. Each point represents a separate Ba⁺ deposit, with the signal averaged over four laser positions separated by 20 μm on the deposit. The error bar is the standard deviation of the four measurements. The observed signal is linear with a log–log slope of 1.04 \pm 0.05. The slope of the linear fit is 379 ± 10 counts per milliwatt-second per ion. Including the uncertainty in the number of ions deposited, the observed fluorescence per ion is 379_{-76}^{+39} counts per milliwatt-second. For these measurements, we used about $40 \,\mu\text{W}$ of focused 572-nm laser excitation with roughly 3 s of laser exposure.

For a practical barium-tagging application in nEXO, it is crucial for each barium tag to be independent of any previous tagging measurements or residual barium on the cryogenic probe, in order to ensure that the barium daughter is correlated to the decay candidate being investigated. To obtain a quantified limit of this 'erasure' property, we plot in Fig. 2b the difference in the background level of the last SXe-only deposit before, and the first SXe-only deposit after, a barium deposit (from Fig. 2a). The data are averaged over four laser positions for each deposit, and the standard deviation is shown as an error bar. The differences are consistent with zero, and the slope of a linear fit— 0.06 ± 0.41

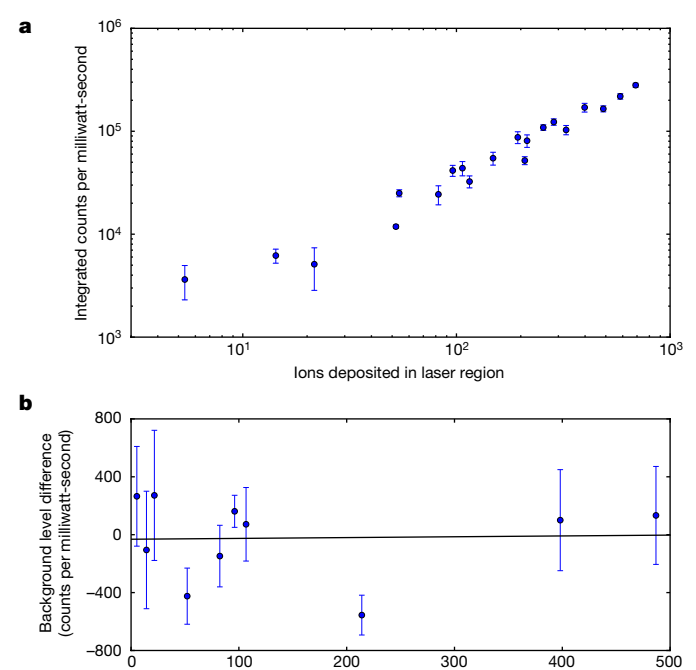


Fig. 2 | **Barium atom fluorescence.** a, The 619-nm fluorescence from barium is plotted against the number of Ba $^+$ ions deposited. The detected CCD counts have been scaled by the laser exposure in milliwatt-seconds. The slope of a log–log fit to the data is 1.04 ± 0.05 (\pm standard deviation). The slope of a linear fit to the data is 379 ± 10 counts per milliwatt-second per ion. **b**, The difference in background level from SXe-only before and after a barium deposit is plotted with respect to the number of barium ions in the deposit. The least-squares fit (black line) has a slope of 0.06 ± 0.41 counts per milliwatt-second per ion. In both panels, the data points are the averages and the error bars are the standard deviations of the four observation locations.

Number of ions in previous deposit

counts per milliwatt-second per ion—is a measure of the barium signal remaining after evaporation. The ratio of the maximum value of the SXe-only difference fit to the minimum barium signal response from the slope of Fig. 2a gives a limit of 0.16% or less on residual barium fluorescence after evaporation.

Scanned images

By further decreasing the density of barium ions deposited, we can spatially resolve single barium atoms. To image these atoms, the laser is rastered across the deposit. A typical scan consists of laser displacements in a square grid of 12×12 steps with 3 s of laser exposure and a spacing of $4\,\mu m$. The raw CCD images of four successive steps of a laser scan are shown in Fig. 3. As the laser passes over the barium atom, a strong 619-nm signal appears. When the laser moves off the barium atom, the observed counts return to background level.

A scan image of this region is generated by integrating the CCD counts in a 4×4 pixel area that encompasses the laser region in each frame. These integrals are divided by the laser exposure, and arranged according to the position of each spot in the grid. Five such scan images, taken from a typical experiment, are shown in Fig. 4. Data from the four frames shown in Fig. 3 contribute to four points on line y=7 in Fig. 4b. In the first SXe-only deposit, no fluorescence peaks are found in the scan (Fig. 4a). After this, the deposit is evaporated by heating the sapphire window to 100 K. Then, a new SXe deposit with 12 pulses of the Ba⁺ ion source, corresponding to 48^{+5}_{-10} Ba⁺ ions in the full scan area, is produced. Two large peaks of roughly equal size in an otherwise low-background area are observed in a scan of this deposit (Fig. 4b). This distinguishes each peak as the location of a single resonant barium atom. This scan is then repeated, and the barium peaks persist, as seen in Fig. 4c.

Fig. 3 | CCD images showing successive steps of a raster scan of a deposit of barium in solid xenon. As the laser moves from left to right, the signal increases abruptly when the laser is positioned at the location of the barium atom. The (x,y) coordinates refer to the laser displacement in

 $4\text{-}\mu\mathrm{m}$ scan steps. Because of the 45° angle of the window, the x- and y- steps on the sample are 4 $\mu\mathrm{m}$ and 5.7 $\mu\mathrm{m}$, respectively. The detected CCD counts have been scaled by the laser exposure in milliwatt-seconds.

At this point, the laser is moved to the location (x, y) = (4.75, 6.00), and many 3-s exposures are taken. Although not intended, this position is not the same as the peak frame (4, 7), but is close to the position of the frame (5, 6). The time dependence of the integrated signal from a 3×3 pixel area of the single barium peak is shown in Fig. 5. The average signal level of 192 counts agrees with the single barium values at this position in the scans—184 and 169 counts, respectively—taking into account 3×3 rather than 4×4 pixel integration. This signal persists for about 30 s of laser exposure, including the previous two scans, before abruptly dropping to the average background level of 21 counts. This discrete turn-off of the fluorescence signal is a hallmark of a single atom.

About 3,300 photons (0.5 CCD counts per photon) are detected from this atom. This corresponds to around 1.4×10^6 photons absorbed and emitted by one atom. For comparison, the standard deviation of the SXe-only background at one laser position in Fig. 5 for a 30-s integration is 47 detected photons. Thus, the fluorescence signal for a single barium atom is 70σ above the background fluctuation at one laser position. For different laser positions in the SXe-only scans (Fig. 4a, e), the background fluctuation standard deviation is 30 detected photons in a 3-s integration. Comparing this with the 330 fluorescence photons detected from a barium atom in 3 s, the barium peaks in a composite image (such as those in Fig. 4b–d) are 11σ above background.

Following this run with a fixed laser position, a third scan is done, and the barium peak on the left has disappeared, as expected. The right-hand barium peak on the edge of the scan persists (Fig. 4d). After evaporating this deposit, a new SXe-only deposit is made. As in the previous SXe-only deposit, no peaks are observed in this scan (Fig. 4e). This illustrates the lack of any 'history effect' due to previous barium deposits and the absence of any signal from possible barium contamination on the sapphire window.

Discussion

The barium sample in this work is deposited as Ba^+ ions. The fluorescence lines of Ba^+ in SXe are expected in the blue-green region rather than the yellow-red region. Thus we favour a spectroscopic assignment of the 619-nm emission line to barium rather than Ba^+ . To further test this, in Fig. 6 we compare a spectrum of a neutral barium deposit made with the barium getter source to a spectrum of a Ba^+ deposit. We observe identical spectra when using the two sources under similar conditions. This confirms that the 619-nm emission line is associated with barium atoms resulting from neutralization of the incident Ba^+ ions. In addition, we observe no fluorescence peak from deposits of Ar^+ ions in SXe at 2,000 eV under similar conditions. This rules out matrix damage as the source of the 619-nm peak.

A reasonable assignment of the 619-nm emission is to barium atoms in a single-vacancy site. The previously studied case of Na⁺ in a solid argon (SAr) matrix is a good analogy. A higher fraction of sodium atoms was found in single-valency sites with Na⁺ ions incident from a laserablation or ion-beam source than with sodium atoms from a thermal atom source¹⁸⁻²¹. In the model presented in ref. ¹⁹, Na⁺ ions preferentially form in single-valency sites in SAr owing to tighter ion binding. Subsequently, some ions are neutralized, resulting in sodium atoms in cramped single-valency sites. Similarly, a barium ion with a Ba⁺Xe equilibrium radius of 3.619 Å (ref. ²²) should prefer a single-valency site with a radius of 4.39 Å in SXe at 50 K (ref. ²³), rather than a larger multivacancy site. After neutralization from Ba⁺ to Ba, the barium atom with a BaXe equilibrium radius of 5.5 Å (refs ^{14,15,22}) is cramped in the single-valency site, but creation of additional vacancies may not be energetically favourable. Below we consider alternative interpretations of barium molecules, and find them to be inconsistent with our observations.

Assignment to Ba_2 is unlikely: Fig. 2a shows a linear (rather than quadratic) relationship between signal and ions deposited. At the low ion density of Fig. 4, implanted Ba^+ ions are separated, on average,

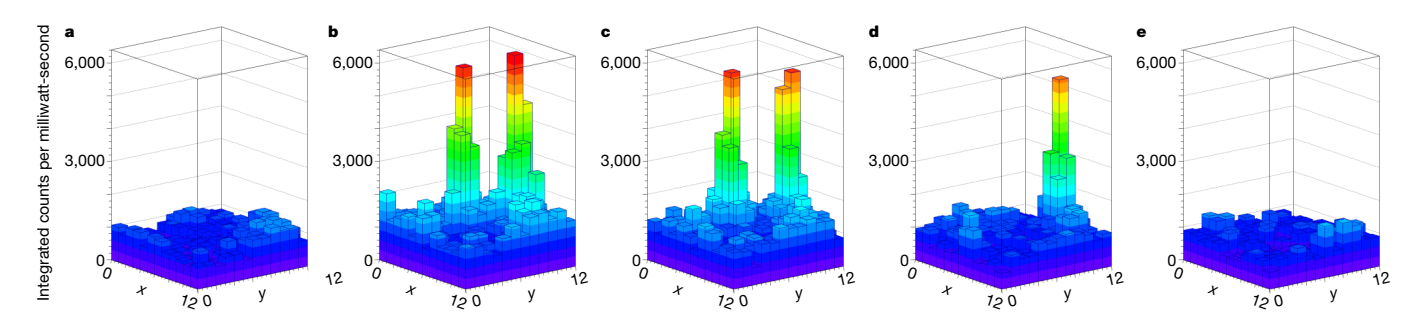


Fig. 4 | **Composite images of a sequence of laser scans.** The laser-displacement step size is 4 μ m, with a 12 \times 12 grid. The integrated CCD counts have been scaled by the laser exposure in milliwatt-seconds. **a**, An SXe-only deposit is made, scanned and evaporated. **b**, **c**, Another deposit is made, of barium in SXe, and scanned twice. **d**, A third scan of the

barium-in-SXe deposit is made after observing the left barium atom peak for 150 s, during which observation its fluorescence disappears. e, The barium-in-SXe sample is evaporated and another SXe-only deposit is made and scanned.

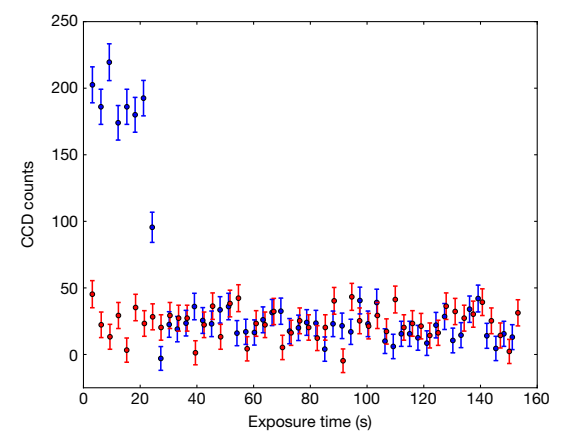


Fig. 5 | Time evolution of the fluorescence signal from a single barium peak. The signal with the laser fixed near the barium atom on the left in Fig. 4 is shown in blue. The signal background from an SXe-only run is shown in red. After about 30 s, the blue signal drops rapidly to the background level, as expected for a single atom. The error bars are the uncertainties from readout noise and photon statistics added in quadrature. In these runs, the average laser exposure per frame is 5.5×10^{-2} milliwatt-seconds.

by 8 μ m. Given that the Ba⁺ ions are implanted 7 \pm 5 nm below the surface of the SXe, mobility of the neutralized barium atoms should be limited²⁴.

We must also consider whether deposited barium reacts with residual gas impurities, such as water and oxygen, to form molecules. However, by comparing fringe rates and partial pressures, we establish that there are less than 100 p.p.m. of residual gas molecules in the SXe matrix. The most likely molecular species that could form are BaOH and BaO, through the reactions:

$$Ba + H_2O \rightarrow BaOH + H$$

 $Ba + O_2 \rightarrow BaO + O$

Both processes are endothermic²⁵, and thus energetically unfavoured. BaOH vapour has known emission bands in the green at 487 nm and 512 nm, and in the infrared at 712–758 nm and 783–839 nm (ref. ²⁶). These do not agree with the observed 619-nm emission. At low temperatures, the upper state of BaO should be primarily the $A^1\Sigma^+$ (ν') state. This state has a multiline spectrum in vacuum with calculated values from 455 to 865 nm (ref. ²⁷). The $\nu'=0$ to $\nu''=2$ and $\nu''=4$ transitions are close to our observed peaks at 619 nm and 670 nm, but adjacent transitions are missing. Furthermore, the excitation spectra of these peaks are different, contradicting a common $\nu'=0$ upper state for the emission (Extended Data Fig. 1). The 356-nm lifetime of the $A^1\Sigma^+$ state in vacuum²⁸ does not fit with the 7-ns decay lifetime for the 619-nm emission line observed here (see Extended Data Fig. 2). Thus, this line is not due to BaO.

Conclusions

We have demonstrated the high-definition imaging and counting of individual barium atoms in solid xenon by scanning a focused laser. The emission peak at 619 nm observed in deposits of Ba⁺ and barium in solid xenon can be attributed to neutral barium atoms in a single-vacancy substitution site. Our observation of two isolated peaks with roughly equal fluorescence in an otherwise low-background area in a scan clearly distinguishes each peak as the location of an individual resonant barium atom. With prolonged laser exposure, the sudden, discrete turn-off of the fluorescence—with signal dropping to background level—is strong confirmatory evidence that the fluorescence is from one atom only. This is, to our knowledge, the first imaging of individual atoms in a solid rare element. Additional features of our study are the very low background obtained by prebleaching the substrate, and the demonstrated limit of 0.16% or less for 'erasure' of the barium signal by

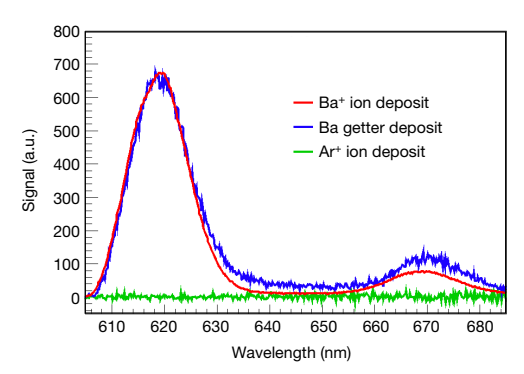


Fig. 6 | Spectra of deposits from three different sources in SXe. The barium getter and Ba⁺ ion beams produce the same fluorescence peaks, which are not produced by matrix damage from an Ar⁺ ion beam. The spectrum of the deposit from the barium getter is scaled because the density of the deposited barium cannot be determined.

deposit evaporation. Successful counting of individual barium atoms in solid xenon is a substantial step towards barium tagging in the nEXO neutrinoless-double- β -decay experiment.

Online content

Any methods, additional references, Nature Research reporting summaries, source data, statements of data availability and associated accession codes are available at https://doi.org/10.1038/s41586-019-1169-4.

Received: 27 June 2018; Accepted: 22 February 2019; Published online 29 April 2019.

- Tanabashi, M. et al. (Particle Data Group) Review of particle physics. Phys. Rev. D 98, 030001 (2018).
- Albert, J. et al. (EXO-200 Collaboration) An improved measurement of the 2νββ half-life of ¹³⁶Xe with EXO-200. Phys. Rev. C 89, 015502 (2014).
- Albert, J. et al. (EXO-200 Collaboration) Search for neutrinoless double-beta decay with the upgraded EXO-200 detector. *Phys. Rev. Lett.* 120, 072701 (2018).
- Moe, M. Detection of neutrinoless double-beta decay. Phys. Rev. C 44, R931 (1991).
- Al Kharusi, S. et al. (nEXO Collaboration) nEXO pre-conceptual design report. https://arxiv.org/abs/1805.11142 (2018).
- Albert, J. et al. (nEXO Collaboration) Sensitivity and discovery potential of nEXO to neutrinoless double beta decay. Phys. Rev. C 97, 065503 (2018).
- Mong, B. et al. Spectroscopy of Ba and Ba⁺ deposits in solid xenon for barium tagging in nEXO. Phys. Rev. A 91, 022505 (2015).
- Twelker, K. et al. An apparatus to manipulate and identify individual Ba ions from bulk liquid Xe. Rev. Sci. Instrum. 85, 095114 (2014).
- Brunner, T. et al. An RF-only ion-funnel for extraction from high-pressure gases. Int. J. Mass Spectrom. 379, 110–120 (2015).
- McDonald, A. D. et al. (NEXT Collaboration). Demonstration of single-barium-ion sensitivity for neutrinoless double-beta decay using single-molecule fluorescence imaging. *Phys. Rev. Lett.* 120, 132504 (2018).
- Wamba, K. Aspects of the R&D for the Enriched Xenon Observatory for Double Beta Decay. PhD Thesis, Stanford Univ. (2006).
- Rowson, P.C. Cryogenic ion capture probe R&D at SLAC. SLAC-PUB-17110 https://www.slac.stanford.edu/pubs/slacpubs/17000/slac-pub-17110.pdf (2017).
- Albert, J. et al. (EXO-200 Collaboration). Measurements of the ion fraction and mobility of alpha and beta decay products in liquid xenon using EXO-200. *Phys. Rev. C* 92, 045504 (2015).
- Davis, B. M. & McCaffrey, J. G. Absorption spectroscopy of heavy alkaline earth metals Ba and Sr in rare gas matrices—CCSD(T) calculations and atomic site occupancies. J. Chem. Phys. 144, 044308 (2016).
- Davis, B. M., Gervais, B. & McCaffrey, J. G. An investigation of the sites occupied by atomic barium in solid xenon—a 2D-EE luminescence spectroscopy and molecular dynamics study. J. Chem. Phys. 148, 124308 (2018).
- Sepiol, J. et al. Detection and spectroscopy of single molecules in rare gas matrices: dibenzanthanthrene in krypton and xenon. *Chem. Phys. Lett.* 311, 29–35 (1999).
- Starukhin, A. et al. Single molecule spectroscopy of Mg-tetrazaporphyrin in xenon matrix. Heavy atom effect. Chem. Phys. 285, 121–126 (2002).
- Tam, S. & Fajardo, M. E. Matrix isolation spectroscopy of metal atoms generated by laser ablation. III. The Na/Ar, Na/Kr, and Na/Xe systems. J. Chem. Phys. 99, 854 (1993).
- Silverman, D. C. & Fajardo, M. E. Matrix isolation spectroscopy of Na atoms deposited as ions. J. Chem. Phys. 106, 8964 (1997).
- Vaskonen, K., Eloranta, J. & Kunttu, H. Trapping of laser-vaporized alkali metal atoms in rare-gas matrices. Chem. Phys. Lett. 310, 245 (1999).

- 21. Ahokas, J., Kiljunen, T., Eloranta, J. & Kunttu, H. Theoretical analysis of alkali metal trapping sites in rare gas matrices. *J. Chem. Phys.* **112**, 2420 (2000).
- Buchachenko, A. A. & Viehland, L. A. Interaction potentials and transport properties of Ba, Ba⁺, and Ba²⁺ in rare gases from He to Xe. J. Chem. Phys. 148, 154304 (2018).
- 23. Granfors, P. R., Macrander, A. T. & Simmons, R. O. Crystalline xenon: lattice parameters, thermal expansion, thermal vacancies, and equation of state. *Phys. Rev. B* **24**, 4753 (1981).
- Ziegler, J. F., Ziegler, M. D. & Biersack, J. P. SRIM—the stopping and range of ions in matter. Nucl. Instr. Meth. Phys. Res. B 268, 1818–1823 (2010).
- 25. Murad, E. Thermochemical properties of the gaseous alkaline earth monohydroxides. *J. Chem. Phys.* **75**, 4080 (1981).
- Charton, M. & Gaydon, A. G. Rotational analysis of the B²Σ⁺-X²Σ⁺ transition of BaOH and BaOD. *Proc. Phys. Soc. A* 69, 520 (1956).
- Sakurai, K., Johnson, S. E. & Broida, H. P. Laser-induced fluorescence of BaO. J. Chem. Phys. 52, 1625 (1970).
- Johnson, S. E. Measured radiative lifetimes and electronic quenching cross sections of BaO(A¹Σ). J. Chem. Phys. 56, 149 (1972).

Acknowledgements We thank Picoquant for the loan of time-resolved-photon-counting equipment. Discussions with J. G. McCaffrey, B. Gervais and A. van Orden are appreciated. This material is based upon work supported by the National Science Foundation under grant number PHY-1649324 and the US Department of Energy, Office of Science, Office of High Energy Physics under award number DE-FG02-03ER41255.

Reviewer information *Nature* thanks Mark Chen, John McCaffrey and the other anonymous reviewer(s) for their contribution to the peer review of this work.

Author contributions The eight authors listed first (C.C., T.W., D.F., A.C., D.R.Y., J.T., A.I. and W.F.) contributed to the design, construction and operation of this experiment, the data acquisition, and the data analysis and interpretation. The remaining authors listed in alphabetical order are nEXO Collaboration members who have contributed to the formulation of the problem and the general application of the results.

Competing interests The authors declare no competing interests.

Additional information

Extended data is available for this paper at https://doi.org/10.1038/s41586-019-1169-4.

Reprints and permissions information is available at http://www.nature.com/reprints.

Correspondence and requests for materials should be addressed to C.C. **Publisher's note:** Springer Nature remains neutral with regard to jurisdictional claims in published maps and institutional affiliations.

© The Author(s), under exclusive licence to Springer Nature Limited 2019

nEXO Collaboration

C. Chambers^{1*}, T. Walton^{1,33}, D. Fairbank¹, A. Craycraft¹, D. R. Yahne¹, J. Todd¹, A. Iverson¹, W. Fairbank¹, A. Alamre², J. B. Albert³, G. Anton⁴, I. J. Arnquist⁵, I. Badhrees^{2,6}, P. S. Barbeau⁷, D. Beck⁸, V. Belov⁹, T. Bhatta¹⁰, F. Bourque¹¹, J. P. Brodsky¹², E. Brown¹³, T. Brunner^{14,15}, A. Burenkov⁹, G. F. Cao^{16,17}, L. Cao¹⁸, W. R. Cen¹⁶, S. A. Charlebois¹¹, M. Chiu¹⁹, B. Cleveland^{20,21}, M. Coon⁸, M. Côté¹¹, W. Cree², J. Dalmasson²², T. Daniels²³, L. Darroch¹⁴, S. J. Daugherty³, J. Daughhetee¹⁰, S. Delaquis^{24,40}, A. Der Mesrobian-Kabakian²⁰, R. DeVoe²², J. Dilling¹⁵, Y. Y. Ding¹⁶, M. J. Dolinski²⁵, A. Dragone²⁴, J. Echevers⁸,

L. Fabris²⁶, J. Farine²⁰, S. Feyzbakhsh²⁷, R. Fontaine¹¹, D. Fudenberg²², G. Gallina¹⁵, G. Giacomini¹⁹, R. Gornea^{2,15}, G. Gratta²², E. V. Hansen²⁵, M. Heffner¹², E. W. Hoppe⁵, J. Hößl⁴, A. House¹², P. Hufschmidt⁴, M. Hughes²⁸, Y. Ito^{14,34}, A. Jamil²⁹, C. Jessiman², M. J. Jewell²², X. S. Jiang¹⁶, A. Karelin⁹, L. J. Kaufman^{3,24}, D. Kodroff²⁷, T. Koffas², S. Kravitz^{22,35}, R. Krücken¹⁵, A Kuchenkov 9 , K. S. Kumar 30 , Y. Lan 15 , A. Larson 10 , D. S. Leonard 31 , G. Li 22 , S. Li 8 , Z. Li 29 , C. Licciardi 20 , Y. H. Lin 25,38 , P. Lv 16 , R. MacLellan 10 , T. Michel 4 , B. Mong²⁴, D. C. Moore²⁹, K. Murray¹⁴, R. J. Newby²⁶, Z. Ning¹⁶, O. Njoya³⁰, F. Nolet¹¹, O. Nusair²⁸, K. Odgers¹³, A. Odian²⁴, M. Oriunno²⁴, J. L. Orrell⁵, G. S. Ortega⁵, I. Ostrovskiy²⁸, C. T. Overman⁵, S. Parent¹¹, A. Piepke²⁸, A. Pocar²⁷ J.-F. Pratte¹¹, D. Qiu¹⁸, V. Radeka¹⁹, E. Raguzin¹⁹, T. Rao¹⁹, S. Rescia¹⁹, F. Retière¹⁵, A. Robinson²⁰, T. Rossignol¹¹, P. C. Rowson²⁴, N. Roy¹¹, R. Saldanha⁵, S. Sangiorgio¹², S. Schmidt⁴, J. Schneider⁴, A. Schubert^{22,36}, K. Skarpaas²⁴ K. Soma²⁸, G. St-Hilaire¹¹, V. Stekhanov⁹, T. Stiegler¹², X. L. Sun¹⁶, M. Tarka²⁷, T. Tolba¹⁶, T. I. Totev¹⁴, R. Tsang⁵, T. Tsang¹⁹, F. Vachon¹¹, B. Veenstra², V. Veeraraghavan²⁸, G. Visser³, J.-L. Vuilleumier³², M. Wagenpfeil⁴, O. Wang¹⁸, J. Watkins², M. Weber²², W. Wei¹⁶, L. J. Wen¹⁶, U. Wichoski²⁰, G. Wrede⁴, S. X. Wu²², W. H. Wu¹⁶, Q. Xia²⁹, L. Yang⁸, Y.-R. Yen^{25,39}, O. Zeldovich⁹, X. Zhang^{16,37}, J. Zhao¹⁶, Y. Zhou¹⁸ & T. Ziegler⁴

¹Physics Department, Colorado State University, Fort Collins, CO, USA. ²Department of Physics, Carleton University, Ottawa, Ontario, Canada. 3Department of Physics and Center for Exploration of Energy and Matter (CEEM), Indiana University, Bloomington, IN, USA. ⁴Erlangen Centre for Astroparticle Physics (ECAP), Friedrich-Alexander University Erlangen-Nürnberg, Erlangen, Germany. ⁵Pacific Northwest National Laboratory, Richland, WA, USA. ⁶King Abdulaziz City for Science and Technology (KACST), Riyadh, Saudi Arabia. ⁷Department of Physics, Duke University, and Triangle Universities Nuclear Laboratory (TUNL), Durham, NC, USA. 8Physics Department, University of Illinois, Urbana-Champaign, IL, USA. 9Institute for Theoretical and Experimental Physics named by A. I. Alikhanov of National Research Center 'Kurchatov Institute', Moscow, Russia. ¹⁰Department of Physics, University of South Dakota, Vermillion, SD, USA. 11 Université de Sherbrooke, Sherbrooke, Québec, Canada. ¹²Lawrence Livermore National Laboratory, Livermore, CA, USA. ¹³Department of Physics, Applied Physics and Astronomy, Rensselaer Polytechnic Institute, Troy, NY, USA. ¹⁴Physics Department, McGill University, Montreal, Québec, Canada. ¹⁵TRIUMF, Vancouver, British Columbia, Canada. ¹⁶Institute of High Energy Physics, Beijing, China. ¹⁷University of Chinese Academy of Sciences, Beijing, China. ¹⁸Institute of Microelectronics Chinese Academy of Science, Beijing, China. 19 Brookhaven National Laboratory, Upton, NY, USA. 20 Department of Physics, Laurentian University, Sudbury, Ontario, Canada. ²¹Sudbury Neutrino Observatory Laboratory (SNOLAB), Sudbury, Ontario, Canada. ²²Physics Department, Stanford University, Stanford, CA, USA. ²³Department of Physics and Physical Oceanography, University of North Carolina Wilmington, Wilmington, NC, USA. ²⁴SLAC National Accelerator Laboratory, Menlo Park, CA, USA. ²⁵Department of Physics, Drexel University, Philadelphia, PA, USA. ²⁶Oak Ridge National Laboratory, Oak Ridge, TN, USA. ²⁷Amherst Center for Fundamental Interactions and Physics Department, University of Massachusetts, Amherst, MA, USA. ²⁸Department of Physics and Astronomy, University of Alabama, Tuscaloosa, AL, USA. ²⁹Department of Physics, Yale University, New Haven, CT, USA. 30 Department of Physics and Astronomy, Stony Brook University, SUNY, Stony Brook, NY, USA. 31 Institute for Basic Science (IBS) Center for Underground Physics, Daejeon, Korea. 32 Laboratory for High Energy Physics (LHEP), Albert Einstein Center, University of Bern, Bern, Switzerland. 33Present address: Prism Computational Sciences, Madison, WI, USA. 34Present address: Japan Atomic Energy Agency (JAEA), Tokai, Japan. ³⁵Present address: Lawrence Berkeley National Lab, Berkeley, CA, USA. ³⁶Present address: Microsoft Corporation, Redmond, WA, USA. ³⁷Present address: Tsinghua University, Beijing, China. ³⁸Present address: Sudbury Neutrino Observatory Laboratory (SNOLAB), Sudbury, Ontario, Canada. ³⁹Present address: Department of Physics, Carnegie Mellon University, Pittsburgh, PA, USA. 40 Deceased: S. Delaquis. *e-mail: chrischambers89@gmail.com

RESEARCH ARTICLE

METHODS

Ba/SXe sample deposition. The source of barium is an ion beam with an energy of 2 keV, filtered to select Ba $^+$ with an electric (E) \times magnetic (B) velocity filter. A set of pulsing plates produces ion bunches of approximately 1 μs for depositing small numbers of ions. The spectra of Ba $^+$ ion deposits in the SXe matrix exhibit peaks known to be due to neutral barium atoms 7 . Thus some percentage of the ions neutralizes in the matrix, although the fraction has not yet been determined. An alternative source of neutral barium is a BaAl $_4$ getter wire, which can be moved into the beam path and heated to emit barium atoms towards the sample. However, it is challenging to achieve low barium flux with this source and to calibrate it.

Deposits are made on a cold sapphire window tilted at 45° with respect to the Ba $^+$ beam. To create a sample, xenon gas is directed towards the window by opening a leak valve. The xenon gas freezes onto the window and forms a SXe matrix with a thickness of around a micrometre. This is initiated a few seconds before the barium deposit, continues during the barium deposit, and is turned off a few seconds after the barium deposit by closing the valve. Thus, the barium atoms are located sparsely in a thin layer at about half the depth of the SXe.

In this work, deposition is carried out with the sapphire window at a temperature of roughly 50 K. This reduces the hydrogen, nitrogen and oxygen content in the matrix, as these residual gases condense at temperatures below 50 K in vacuum 7 . The window is then cooled to 11 K for observation. Xenon is deposited at a rate of around 60 nm s $^{-1}$. An experiment cycle consists of a deposition at 50 K, a fluorescence observation at 11 K, and then evaporation of the deposit by heating the window to 100 K. Many deposits are made in a day with varying numbers of ions deposited, as well as periodic SXe-only deposits to establish the background.

Measurement of Ba⁺ ion density. The area density of deposited Ba⁺ ions cannot be measured directly because the window is an insulator. During the deposit, only the induction signal of the pulse of ions in transit through a circular induction plate is recorded. To estimate the deposited ion density, the pulsed ion beam is sampled before and after deposits by two Faraday cups located 17.5 cm and 4.5 cm before the window. The factor for conversion of these signals to ion density on the window is measured in a separate calibration procedure, in which the window is replaced by a third Faraday cup at the window position, and the alignments and magnitudes of the three cup signals are compared under conditions similar to those of actual deposits. The uncertainty in the Faraday cup measurements is estimated as \pm 10% owing to secondary electron effects, measured by biasing the Faraday cup electrodes. An additional +0% to -10% uncertainty in the ion density deposited on the observation window is included to take into account a possible 1 mm misalignment of the approximately Gaussian ion beam, with a full width at half maximum of 5.1 mm, relative to the excitation laser. Conservatively adding these uncertainties linearly, the total uncertainty in Ba⁺ ion density at the window is +10% to -20%.

The number of Ba⁺ ions deposited within the 1/e radius of the laser beam gives a rough upper limit to the number of barium atoms responsible for the observed signal with a fixed laser beam. For typical ion-bunch densities of 0.1–1 fC mm⁻² and focused laser 1/e radii of $w_{0x} = 3.2 \, \mu \text{m}$ and $w_{0y} = 3.8 \, \mu \text{m}$, this results in about 0.001– $0.01 \, \text{Ba}^+$ ions per pulse in the 1/e intensity laser region.

Excitation laser system. The excitation laser, a Coherent 599 cw dye laser with rhodamine 6G dye, pumped by the 532-nm line of a Coherent Verdi-V8 laser, enters from the back side of the window. To position the laser beam with submicrometre precision, we used two computer-controlled piezoelectric translation stages to move the laser focusing lens. Barium fluorescence light is collected and collimated by a 50-mm Nikon camera lens. A filter with a sharp-edged band-pass of 610–630 nm passes just the 619-nm fluorescence peak. A 200-mm Nikon camera lens then focuses the light onto a liquid-nitrogen-cooled CCD (Roper Scientific SPEC-10 liquid-nitrogen-cooled spectroscopy detector), resulting in an image of $\times 4$ magnification. Each of the 20 $\mu m \times 20~\mu m$ pixels of the CCD represents an area of approximately 5 $\mu m \times 7~\mu m$ on the SXe sample, which is at tilted at 45° in the y-direction.

For a given laser intensity, the smallest focus possible is desired for an optimal signal-to-background ratio from single atoms. To achieve this, we used an aspherical lens with a focal length of 7.9 cm (Thorlabs, part ASL10142-A) to minimize spherical aberration, and placed a fused silica optical flat with a thickness of 1 cm at 9° after the lens in order to compensate for astigmatism caused by the tilted sapphire window.

Vibrations of the sapphire window relative to the excitation laser increase the area of laser exposure, and reduce the average intensity seen by a single barium atom. The main source of vibration is the cryostat helium compressor cycle, which pulses with a frequency of about 2.25 Hz. To limit the laser exposure to a segment of the cryostat cycle with minimal vibration, a shutter is placed in the laser path and synchronized with the signal from an accelerometer on the outside of the cryostat. This laser gating has a 45% duty cycle.

Backgrounds for 619-nm emission. A typical CCD image recorded with a focused laser beam at 570 nm is shown in Extended Data Fig. 3. A strong signal from the barium deposit in SXe on the front surface of the window is visible. A Gaussian fit to the image gives a $1/e^2$ radius of $10.4 \, \mu m$, which is larger than the average laser beam radius of $w = 3.5 \, \mu m$. Aberrations and vibrations in the collection optics and imperfections in the surface of the SXe layer contribute to blurring of the image. A weak background emission from the opposite window surface is also visible.

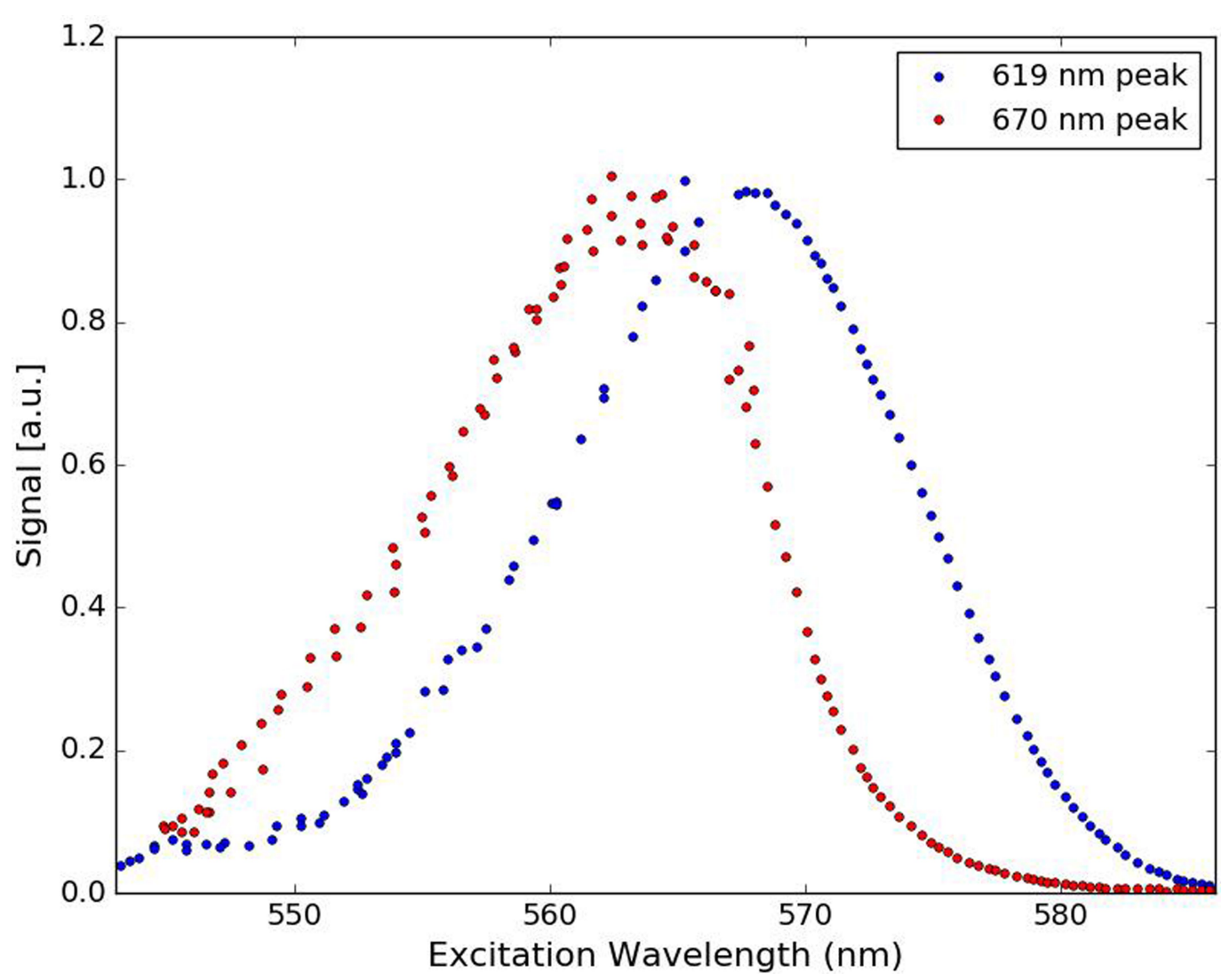
Very low concentrations of Cr^{3+} in the sapphire bulk (sub-p.p.b. level) produce a sharp fluorescence peak at 693 nm, with a broad tail extending to the 610–630-nm region passed by the band-pass filter. This results in the faintly visible line through the window in the CCD image. Commercially available c-plane quality sapphire from Meller Optics and Rubicon Technologies has been found to have sufficiently low Cr^{3+} concentrations for detecting single barium atoms.

The background emission from the front sapphire surface beneath the SXe layer is the main challenge for single-barium imaging. It has been found that this background can be reduced substantially and semipermanently by photobleaching. A variety of wavelengths have been used effectively for bleaching, including 514.5 nm, 532 nm, 570–572 nm and 580.5 nm. A typical bleaching procedure consists of a repeating raster scan of an 80-mW, 532-nm laser, focused to around $w_0=10~\mu\text{m}$, in a 14×14 position grid, with 8- μm grid spacing and 20 s duration at each position per scan. This is done with the sapphire window at 100 K. As seen in a subsequent imaging scan (Extended Data Fig. 4), this reduces the surface background by about 30× over a region of about 90 $\mu\text{m} \times 90~\mu\text{m}$. This area is large enough to accommodate both the fixed laser and the scanned images presented in the section 'Scanned images' in the main text.

Time-resolved photon counting. The decay lifetimes of both the sapphire surface background and the average signal from many barium atoms were investigated using a 561-nm pulsed laser with 100-ps pulse length as the excitation source, and a single photon avalanche photodiode (SPAD) as the detector. The time between the laser pulse and the arrival of a photon at the SPAD was measured by a fast counter, and a histogram of photon arrival times was recorded (Picoquant PicoHarp 300, PDL800D laser and PDM detector). The decay histograms for an SXe-only (green) and barium-in-SXe (blue) deposit are shown in Extended Data Fig. 2. By subtracting the SXe-only histogram from the barium histogram, we isolated the decay lifetime for the 619-nm emission of barium and measured it to be 7.0 \pm 0.3 ns. The SXe-only background decay comprises more than one decay constant, but is nonetheless much shorter than the barium decay lifetime. By time gating the CCD or SPAD, the signal-to-background ratio can be increased by a factor of two with a loss of 50% of the barium signal. In the future, a sapphire window will be mounted at the end of a cryoprobe⁷, likely to be made of stainless steel. Background emission from the metal tubing may be a concern for barium atom detection. The observed lifetime of emission at 619 nm from a stainless-steel cryoprobe tube (Extended Data Fig. 2, red), is about 1.5 ns. Thus, background from the stainless-steel parts of a cryoprobe could be reduced by time gating with minimal barium signal loss.

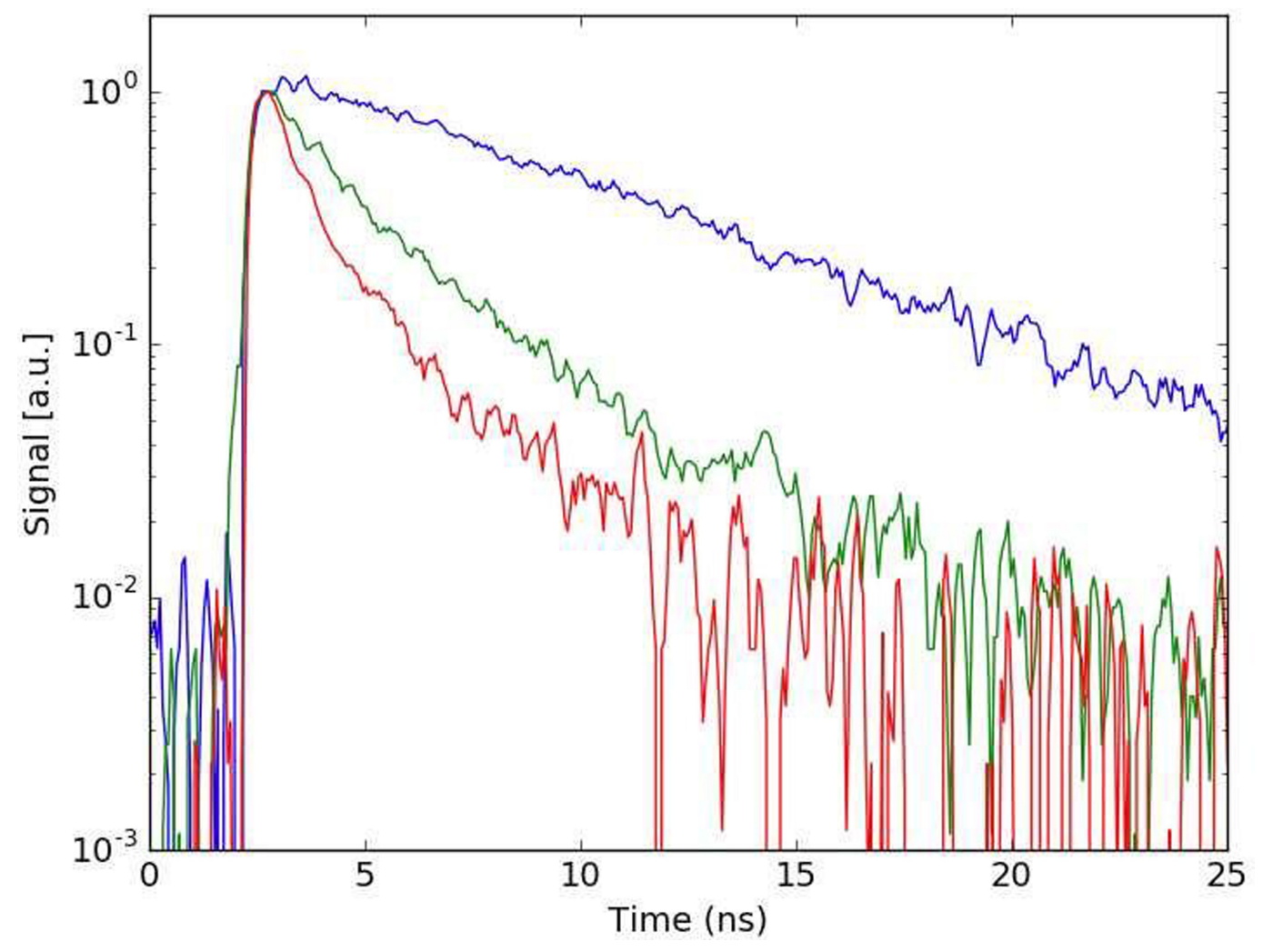
Data availability

Source Data for Figs. 2-6 are provided with the online version of the paper.



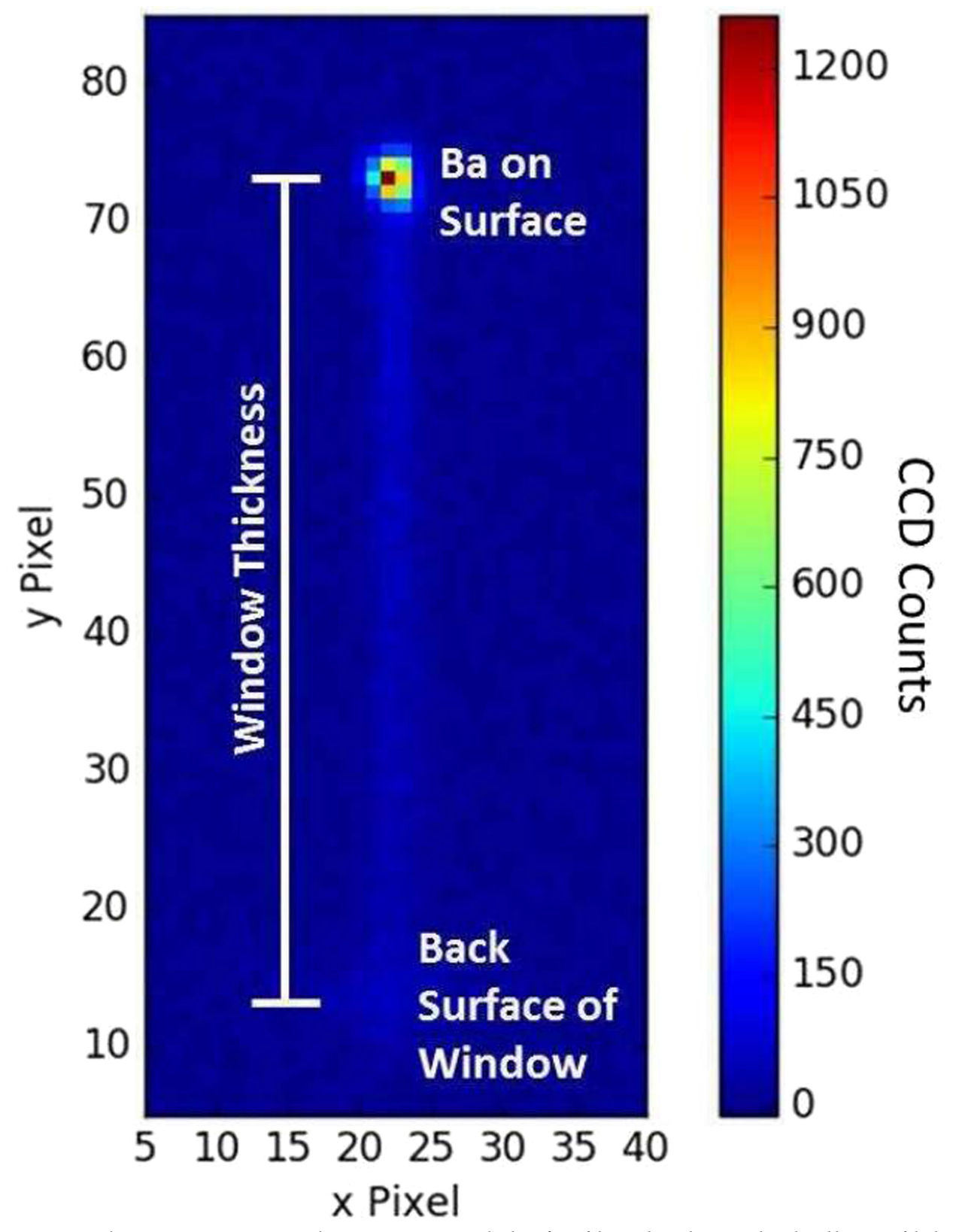
Extended Data Fig. 1 | Excitation spectra for emission at 619 nm and 670 nm. These spectra were obtained with deposits of high barium density and with low laser intensity in order to avoid bleaching effects. The low wavelength portion (below 567 nm) was excited using rhodamine-100 laser dye, and the high wavelength portion (above 567 nm) was excited

using rhodamine-6G laser dye. The two portions were normalized, because the laser intensity and barium densities were different for the two experiments. The shapes of the spectra are similar and do not exhibit resolved Jahn–Teller splitting. The peak locations differ, indicating that the emissions do not originate from a shared upper state.



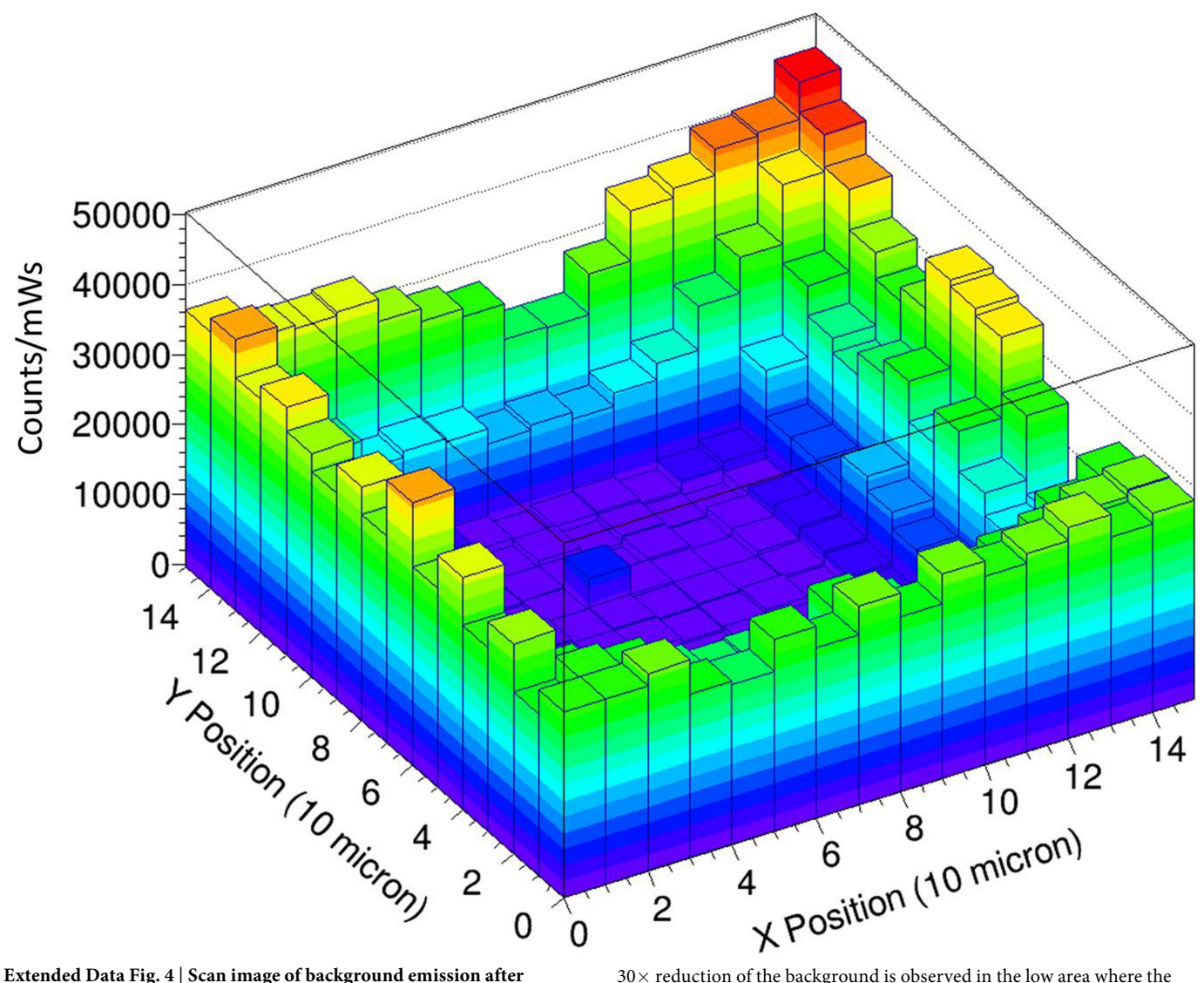
Extended Data Fig. 2 | Time-resolved photon counting of 619-nm fluorescence. Histograms showing the decay of the 619-nm fluorescence for barium in SXe (blue), SXe-only (green) and the cryoprobe tube (red).

The decay lifetime of the barium fluorescence is 7.0 ± 0.3 ns. The SXe-only and cryoprobe emissions have shorter decay lifetimes of approximately 3 ns and 1.5 ns respectively.



Extended Data Fig. 3 | Example CCD image of a Ba $^+$ deposit in SXe. The barium atoms were excited by a focused 570-nm laser, using a 620-nm fluorescence band-pass filter. The bright spot at the top of the image is the front surface of the window on which the Ba $^+$ ions were deposited. The broad spot at the bottom of the image is the surface fluorescence of the

back surface of the window. This spot is broadened because of the laser focus as well as the collection optics being optimized for the front surface. The faint line between the surfaces is the faint fluorescence of Cr^{3+} impurities in the bulk of the sapphire that extends into the wavelength region of the filter.



Extended Data Fig. 4 | Scan image of background emission after bleaching. We used a 532-nm laser to bleach the sapphire surface background in a 14 \times 14 grid pattern with 8- μm steps. A roughly

 $30\times$ reduction of the background is observed in the low area where the bleaching laser was scanned.